

Oxidative desulfurization pathway for complete catabolism of sulfoquinovose by bacteria

Mahima Sharma,¹ James P. Lingford,^{2,3} Marija Petricevic,^{4,5} Alexander J.D. Snow,¹ Yunyang Zhang,^{4,5} Michael A. Järvå,^{2,3} Janice W.-Y. Mui,^{4,5} Nichollas E. Scott,⁶ Eleanor C. Saunders,⁷ Runyu Mao,^{2,3} Ruwan Epa,^{4,5} Bruna M. da Silva,^{7,8} Douglas E.V. Pires,^{7,8} David B. Ascher,^{5,7} Malcolm J. McConville,⁷ Gideon J. Davies,^{1*} Spencer J. Williams,^{4,5*} Ethan D. Goddard-Borger^{2,3*}

¹ York Structural Biology Laboratory, Department of Chemistry, University of York, Heslington, YO10 5DD, U.K.

² The Walter and Eliza Hall Institute of Medical Research, Parkville, Victoria 3052, Australia.

³ Department of Medical Biology, University of Melbourne, Parkville, Victoria 3010, Australia.

⁴ School of Chemistry, University of Melbourne, Parkville, Victoria 3010, Australia.

⁵ Bio21 Molecular Science and Biotechnology Institute, University of Melbourne, Parkville, Victoria 3010, Australia

⁶ Department of Microbiology and Immunology, University of Melbourne at the Peter Doherty Institute for Infection and Immunity, Parkville, Victoria 3010, Australia.

⁷ Department of Biochemistry and Pharmacology, Bio21 Molecular Science and Biotechnology Institute, University of Melbourne, Parkville, Victoria 3010, Australia

⁸ School of Computing and Information Systems, University of Melbourne, Melbourne, Victoria 3010, Australia

Keywords: carbohydrate metabolism, sulfur cycle, oxidative desulfurization

*Correspondence and requests for materials should be addressed to G.J.D. (gideon.davies@york.ac.uk), S.J.W. (sjwill@unimelb.edu.au) or E.D.G.-B. goddard-borger.e@wehi.edu.au.

30 *Abstract*

31 Catabolism of sulfoquinovose (SQ, 6-deoxy-6-sulfoglucose), the ubiquitous sulfosugar produced by
32 photosynthetic organisms, is an important component of the biogeochemical carbon and sulfur cycles.
33 Here, we describe a new pathway for SQ degradation that involves oxidative desulfurization to
34 release sulfite and enable utilization of the entire carbon skeleton of the sugar to support the growth
35 of the plant pathogen *Agrobacterium tumefaciens*. SQ or its glycoside sulfoquinovosyl glycerol
36 (SQGro) are imported into the cell by an ABC transporter system with an associated SQ binding
37 protein. A sulfoquinovosidase hydrolyses the SQ glycoside and the liberated SQ is acted on by a
38 flavin mononucleotide-dependent sulfoquinovose monooxygenase, in concert with an NADH-
39 dependent flavin reductase, to release sulfite and 6-oxo-glucose. An NADPH-dependent
40 oxidoreductase reduces the 6-oxo-glucose to glucose, enabling entry into primary metabolic
41 pathways. Structural and biochemical studies provide detailed insights into the recognition of key
42 metabolites by proteins in this pathway. Bioinformatic analyses reveal that the sulfoquinovose
43 monooxygenase (smo) pathway is distributed across Alpha- and Betaproteobacteria and is especially
44 prevalent within the Rhizobiales order. This strategy for SQ catabolism is distinct from previously
45 described pathways as it enables the complete utilization of all carbons within SQ by a single
46 organism with concomitant production of inorganic sulfite.

47

48

49 *Significance Statement*

50 Sulfoquinovose, a sulfosugar derivative of glucose, is produced by most photosynthetic organisms
51 and contains up to half of all sulfur in the biosphere. Several pathways for its breakdown are known,
52 though they provide access to only half of the carbon in sulfoquinovose and none of its sulfur. Here,
53 we describe a fundamentally different pathway within the plant pathogen *Agrobacterium tumefaciens*
54 that features oxidative desulfurization of sulfoquinovose to access all carbon and sulfur within the
55 molecule. Biochemical and structural analyses of the pathway's key proteins provided insights how
56 the sulfosugar is recognized and degraded. Genes encoding this sulfoquinovose monooxygenase
57 pathway are present in many plant pathogens and symbionts, alluding to a possible role for
58 sulfoquinovose in plant host–bacteria interactions.

59

60 **Introduction**

61 Sulfoquinovose (SQ; 6-deoxy-6-sulfoglucose) is an anionic sulfosugar found in plant and
62 cyanobacterial sulfolipids, and in S-layer proteins in archaea (1). It is estimated that SQ holds around
63 half of all sulfur in the biosphere, with 10 billion tonnes produced each year in Nature, and so its
64 cycling is a significant component of the biogeochemical sulfur cycle (2). Microbial communities
65 play a dominant role in SQ cycling and usually more than one organism is required to completely
66 assimilate this source of carbon and sulfur. Organisms with a tier 1 pathway, termed sulfoglycolysis,
67 perform scission of the C3-C4 bond of SQ to give two three-carbon fragments; carbons 1-3 enter
68 central metabolism, while carbons 4-6 bearing the sulfonate are excreted as
69 dihydroxypropanesulfonate (DHPS) or sulfolactate (SL). Organisms with a tier 2 pathway are those
70 that process DHPS and SL to access the remaining three carbon fragment and release inorganic sulfur.
71 To date, three tier 1 pathways have been described: the sulfoglycolytic Embden-Meyerhof-Parnas
72 (sulfo-EMP) (3), Entner-Doudoroff (sulfo-ED) (4, 5) and sulfofructose transaldolase (sulfo-SFT)
73 pathways (6, 7). Tier 2 metabolism has been described for various specialized bacteria that utilize SL
74 or DHPS and perform ‘biomineralization’ to release inorganic sulfite, which under aerobic conditions
75 is readily oxidized to sulfate (1). While many of the steps in the three tier 1 sulfoglycolysis pathways
76 differ, all three pathways share the presence of a specialized glycoside hydrolase, a
77 sulfoquinovosidase (SQase), which catalyzes the hydrolysis of SQ glycosides, such as SQGro, to
78 release SQ (8, 9).

79
80 While the tier 1 and 2 pathways described to date require two or more organisms to complete the
81 ‘biomineralization’ of SQ, there is some evidence that this can also be accomplished by a single
82 organism. Roy and co-workers have reported that an *Agrobacterium* strain from soil can completely
83 consume SQ, with release of sulfate, although the genetic and biochemical details behind this process
84 were not investigated (10). We previously reported that *A. tumefaciens* C58 contains a functional
85 SQase, with the ability to hydrolyze SQGro (8). However, analysis of its genome did not reveal any
86 genes homologous to those expected for known tier 1 sulfoglycolysis pathways.

87
88 Here, we investigate the ‘biomineralization’ of SQ by *Agrobacterium tumefaciens* (*Agrobacterium*
89 *fabrum*) strain C58 and show that this organism effects the oxidoreductive desulfurization of SQ to
90 release inorganic sulfite and glucose, which can feed into primary metabolism. We show that this
91 pathway involves: a novel SQ/SQGro solute binding protein and associated ATP-binding cassette
92 (ABC) transporter; an SQase to release SQ from its glycosides; a flavin-dependent SQ
93 monooxygenase with paired flavin-reductase to effect oxidative desulfurization of SQ to sulfite and
94 6-oxo-glucose; and a NADPH-dependent oxidoreductase to reduce 6-oxo-glucose to glucose. X-ray

95 structures determined for each of these proteins in complex with relevant metabolites reveal the
96 molecular basis of substrate binding and catalysis. We show through bioinformatics analyses that this
97 pathway – the first to enable the complete assimilation of SQ – is distributed across Alpha- and
98 Betaproteobacteria and is particularly well-represented within the Rhizobiales order.
99

Results

Differential expression of a gene cluster in the presence sulfoquinovose

To determine if *A. tumefaciens* C58 can utilize SQ as a carbon source, we attempted to grow this organism in M9 minimal media containing SQ as the sole carbon source. *A. tumefaciens* C58 exhibited robust growth in this media and analysis of spent culture supernatant failed to detect DHPS or SL. Instead, the culture supernatant accumulated sulfate, but with a lag between consumption of SQ and sulfate release (**Fig. 1a**), as was previously reported by Roy and co-workers for *Agrobacterium* sp. strain ABR2 (10). Noting that sulfite is generally released from organosulfonate degradation pathways (1, 11), we analyzed the supernatant for sulfite (SO_3^{2-}), and observed that SQ consumption is coincident with production of sulfite, which slowly undergoes autooxidation to sulfate. To investigate the metabolism of the carbon skeleton of SQ, we cultured *A. tumefaciens* on $^{13}\text{C}_6$ -SQ (12) and analyzed the culture supernatant using ^{13}C NMR spectroscopy (**Fig. S1**). The only significant ^{13}C -labelled product we could detect was ^{13}C -bicarbonate, which formed transiently during exponential phase growth, and the ^{13}C -labelled bicarbonate signal disappeared at stationary phase, presumably through exchange with atmospheric CO_2 . *A. tumefaciens* grew on other sulfoquinovosides, including SQGro and methyl α -sulfoquinovoside (MeSQ), but did not grow on other alkylsulfonates including DHPS, SL, sulfoacetic acid, taurine, pentanesulfonate, MES, MOPS, HEPES, PIPES, cysteic acid or methanesulfonic acid (**Fig. S2**). Collectively, this data demonstrates that *A. tumefaciens* effects the complete metabolism of the carbon backbone of SQ with concomitant release of sulfite.

We performed comparative proteomic experiments to identify changes associated with the growth of *A. tumefaciens* on SQ compared to glucose at mid-log phase (**Fig. 1b**). The largest and most significant change we observed was an increase in the abundance of proteins encoded by a single cluster of genes (*Atu3277-Atu3285*) for cells grown on SQ. Proteins encoded by *Atu3283* and *Atu3284* were not observed; however, they are predicted to be integral membrane proteins that can be difficult to detect using conventional proteomic workflows (13). Thus, the gene cluster *Atu3277-Atu3285*, which was subsequently renamed *smoA-smoI*, appeared to be important for growth on SQ (**Fig. 1c**). While the protein encoded by *Atu3285* was previously identified as an SQase (8), the proteins encoded by other genes in the cluster were not annotated with functions that were consistent with any tier 1 pathway, suggesting that *A. tumefaciens* uses a different approach for the catabolism of SQ. The automated annotations ascribed to the respective gene products in the cluster, which included a putative ABC transporter system, sulfonate monooxygenase, SDR oxidoreductase, flavin reductase and exporters, enabled development of a hypothetical biochemical pathway that could explain the

complete assimilation of SQ by *A. tumefaciens* (**Fig. 1d**). We proceeded to biochemically validate this hypothesis and gain structural insights into the proteins involved.

136

137 *Atu3282 (smoF) encodes an ABC transporter solute-binding protein that binds SQGro*

138 Within the gene cluster identified through proteomics, *Atu3281 (smoE)*, *Atu3283 (smoG)*, and
139 *Atu3284 (smoH)* were annotated as an ABC transporter system, with *Atu3282 (smoF)* encoding an
140 associated periplasmic solute-binding protein. The substrate preferences of solute binding proteins
141 are useful for assigning functions to their associated ABC transporters (14). Accordingly, we
142 produced recombinant SmoF (**Fig. S3**) and demonstrated that it binds SQGro with $K_d = 290$ nM (ΔH
143 $= -11$ kcal mol⁻¹, $\Delta S = -7$ cal mol⁻¹ deg⁻¹) (**Fig. 2a, Table S3**). No binding was observed for the
144 stereochemically-related monosaccharides D-glucose and D-glucuronic acid.

145

146 To delineate how SmoF recognizes its ligand, we used X-ray diffraction methods to obtain a high-
147 resolution 3D structure of SmoF in its ligand-free apo state and in complex with SQGro (**Fig. 2b,**
148 **Table S4**). Like most ABC transporter solute-binding proteins, SmoF possesses two globular
149 domains with a similar α/β fold forming a deep cleft lined with aromatic and polar residues to capture
150 the ligand. Comparisons of the structures for ligand-free SmoF and the SQGro complex revealed a
151 large conformational change in the protein resulting from inter-domain rotation upon SQGro binding.
152 The relative movement of domains was assessed using the DynDom server, which indicated a hinge
153 rotation of 31° about four linker regions connecting the two domains (**Fig. S4**). SQGro is buried deep
154 within the inter-domain cleft and residues from both domains accommodate this ligand through a
155 network of hydrogen-bonding interactions (**Fig. 2c,d**). The sulfonate of SQGro, which is the defining
156 feature of this sulfosugar, is accommodated by hydrogen-bonds to the side-chain of Thr220 (2.6 Å),
157 backbone amides of Gly166 (3 Å) and Ser43 (2.8 Å), and an ordered water molecule that in turn
158 hydrogen-bonds to the sidechain of His13 (3 Å) and Gln46 (3.2 Å) (**Fig. 2c,d**). These and the other
159 interactions in the SQGro-bound ‘closed’ state stabilized SmoF substantially, as evidenced by a 15
160 °C increase in the protein melting temperature (**Fig. S5**).

161

162 *The structural basis of SQGro recognition by the SQase Atu3285 (SmoI)*

163 We previously reported that *Atu3285 (smoI)* encodes an SQase that preferentially hydrolyses 2'*R*-
164 SQGro, the natural stereoisomer of this glycoside (8). To understand the molecular basis of the
165 preference SmoI has for this stereoisomer, we determined the 3D structure of a pseudo-Michaelis
166 complex: the inactive acid/base mutant SmoI-D455N in complex with 2'*R*-SQGro (**Fig. 2e,f**). SmoI-
167 D455N•SQGro crystallized with four protomers in the asymmetric unit, each showing unambiguous
168 density of the substrate bound at the active site. As described previously, the overall fold is an $(\alpha/\beta)_8$

169 barrel appended with small β sheet domain and the sulfonate group is recognized by
170 Arg283/Trp286/Tyr491 triad⁸. Arg438 and Glu135 make hydrogen-bonding interactions with the
171 glyceryl aglycone of 2'R-SQGro. Only Arg438 interacts with the C2-hydroxyl group of the glyceryl
172 aglycone and thus this residue appears to drive selectivity for the 2'R-SQGro stereoisomer.

173
174 ***Atu3277 (smoA) encodes a flavin mononucleotide (FMN) reductase***

175 SmoA, annotated as a flavin reductase, was recombinantly expressed in *E. coli* and maintained a
176 yellow color throughout purification, suggesting that it had co-purified with a flavin co-factor. A
177 sample of this protein was heat-denatured to release the co-factor and the supernatant analyzed by
178 LC-MS to reveal that FMN was the sole detectable flavin (**Fig. S6**). Michaelis-Menten kinetics were
179 conducted for SmoA with saturating FMN and NADH or NADPH to determine which of these
180 reductants was preferred by the enzyme. With NADH the kinetic parameters were $K_M = 35 \pm 5 \mu\text{M}$,
181 $k_{\text{cat}} = 14.5 \pm 0.5 \text{ s}^{-1}$ and $k_{\text{cat}}/K_M = 4.1 \times 10^5 \text{ M}^{-1} \text{ s}^{-1}$; while for NADPH saturation was not observed and
182 $k_{\text{cat}}/K_M = 6.8 \times 10^2 \text{ M}^{-1} \text{ s}^{-1}$, indicating that NADH is the preferred cofactor for SmoA (**Fig. 3a, Fig. S7**).
183 Owing to difficulties in obtaining structural data for this enzyme, we also studied a close homologue
184 from *Rhizobium oryzae* (RoSmoA, UniProt accession number: A0A1X7D6Q3), which possesses a
185 syntenic gene cluster to *Atu3277-Atu3285*. Recombinant RoSmoA also co-purified with FMN (**Fig.**
186 **S6**) and utilized the NADH cofactor with $K_M = 16 \mu\text{M}$, $k_{\text{cat}} = 33 \text{ s}^{-1}$ and $k_{\text{cat}}/K_M = 2.1 \times 10^6 \text{ M}^{-1} \text{ s}^{-1}$
187 (**Fig. S7**).

188
189 ***Atu3279 (smoC) encodes an SQ monooxygenase that desulfurizes SQ***

190 SmoC is annotated as an alkanesulfonate monooxygenase, though it possesses only 30% sequence
191 identity with the well-characterized alkanesulfonate monooxygenase SsuD, from *E. coli*. SsuD
192 catalyzes the FMNH₂- and O₂-dependent oxidation of alkanesulfonates to produce the corresponding
193 aldehyde and sulfite, with a preference for pentanesulfonate (15). The mechanism of this and related
194 enzymes have been intensively studied yet remain enigmatic. The transformation is thought to involve
195 initial formation of a C4a-peroxy or N5-peroxy flavin species on-enzyme. One mechanism posits that
196 the terminal peroxide oxygen attacks the sulfonate sulfur of the substrate before undergoing a
197 rearrangement to effect C-S bond fissure and release of the aldehyde and sulfite products (**Fig. S8a**)
198 (16). An alternative mechanism suggests the peroxide deprotonates C6, which is then oxidized to an
199 α -hydroxysulfonate that undergoes elimination to produce sulfite and the aldehyde (17). To
200 demonstrate activity for recombinant SmoC (**Fig. S3**), we adapted assays developed for SsuD that
201 use Ellman's reagent to detect sulfite released by the enzyme (18). Direct detection of the putative
202 sugar product, 6-oxo-glucose (6-OG), is not trivial as this molecule exists as a complex equilibrium
203 of (hemi)acetals and hydrates that have poor stability. Thus, SmoC was incubated with SQ in the

204 presence of SmoA, FMN and NADH, which generate FMNH₂ *in situ*, and the concentration of sulfite
205 determined periodically using Ellman's reagent (**Fig. 3b**). Maximal substrate conversion was
206 approximately 200 μ M, which is commensurate with the solubility of molecular oxygen in water
207 under standard conditions, with peak activity observed at pH 8.5 (**Fig. S8**). No activity was observed
208 when SQ was replaced with other sulfonates, including SQGro (the precursor to SQ) or HEPES (an
209 unrelated sulfonate) demonstrating that, unlike the promiscuous SsuD, SmoC has high specificity for
210 SQ. As such, the hydrolysis of SQGro by SmoI necessarily precedes oxidative desulfurization by
211 SmoC. This observation is further supported by ITC, where SQ was found to bind SmoC with K_d =
212 3 μ M in the absence of any flavin-based cofactors, whereas no binding was detected for SQGro (**Fig.**
213 **3c, Table S3**). The unique SQ monooxygenase activity of SmoC defines this pathway: it is the
214 enzyme that effects fission of the C–S bond in SQ, and so it was chosen as the namesake for this gene
215 cluster and *Atu3277-Atu3285* were renamed the SQ MonoOxxygenase cluster (*smoA-I*).
216

217 While we could readily crystallize SmoC, these crystals only diffracted to a maximum resolution of
218 3.4 Å. The corresponding low-resolution map suggested that SmoC exists as a dimer, which was
219 confirmed in solution by SEC-MALS (**Fig. S9**). To obtain structural information for an SQ
220 monooxygenase, we turned to the homolog from *R. oryzae* (*RoSmoC*). Recombinant *RoSmoC*
221 exhibited similar activity and substrate selectivity for SQ to SmoC (**Fig. S8**) and provided crystals
222 that diffracted to 1.9 Å. Importantly, the low-resolution structure of *A. tumefaciens* SmoC
223 superimposed with the high-resolution *RoSmoC* structures with a peptide backbone rmsd of 0.4 Å
224 across the entire structure, providing confidence that both enzymes shared a common structure and
225 function (**Fig. S10**). Both SQ monooxygenases consist of a core (α/β)₈ TIM barrel with three
226 additional insertion regions, analogous to monooxygenases from the bacterial luciferase family. The
227 protomers exist as a homodimer that buries 4697 Å² of surface area, amounting to 18% of total
228 accessible surface area for each protomer (**Fig. 3d**). Pairwise structural analysis using the DALI
229 server identified close relationships to a putative luciferase-like monooxygenase (3RAO.pdb) with
230 an rmsd of 2.4 over 314 residues and a Z score of 34.3, the FMNH₂-dependent methanesulfonate
231 monooxygenase MsuD (7K14.pdb, rmsd 2.0/322 residues, Z-score of 41.0), and the FMNH₂-
232 dependent alkanesulfonate monooxygenase SsuD (1M41.pdb, rmsd 1.8/317 residues, Z-score of
233 41.2).
234

235 Comparisons of the *RoSmoC* structure with MsuD (7K14.pdb) in complex with FMN enabled
236 identification of the FMN binding site *RoSmoC*: a deep hydrophobic pocket that accommodates
237 the isoalloxazine ring system and extends out to the protein-solvent interface, which is gated by
238 conserved phosphate-binding residues Tyr136 and Ser189 (**Fig. 3e**) (17). The close structural and

functional relationship of RoSmoC to MsuD is evident from the conservation of a putative sulfonate binding site comprised of the side-chains Trp206, Arg236, His238, Tyr341 and His343 (**Fig. 3f**) (17). Aside from conferring these enzymes with an ability to bind sulfonates, these conserved active-site residues have been suggested to contribute to the stabilization of a peroxyflavin intermediate in MsuD and SsuD (17, 18). Efforts to obtain crystals of a RoSmoC–SQ complex were unsuccessful, limiting further insights into the origin of enzyme specificity towards SQ over other sulfonates.

Atu3278 (smoB) encodes an oxidoreductase that converts 6-oxo-glucose to glucose

SmoB is annotated as a short-chain dehydrogenase/reductase (SDR) and we had hypothesized that it was responsible for reduction of 6-OG to glucose (**Fig. 1d**). Since 6-OG is difficult to study directly, we tested our hypothesis by looking for SmoB-mediated isotope incorporation into glucose at equilibrium (**Fig. 4a**). Assuming our hypothesis to be true, and as a consequence of microscopic reversibility, incubation of SmoB with a nicotinamide co-factor and glucose in H₂¹⁸O should result in transient formation of 6-OG, rapid and reversible hydration/dehydration with H₂¹⁸O to compete-out ¹⁶O at C6 for ¹⁸O, and reduction to give 6-¹⁸O-glucose. In parallel to this process, ¹⁸O incorporation will occur at C1 of glucose through a similar series of hydration/dehydration reactions. Before proceeding with these experiments, we used ITC to establish which nicotinamide cofactor was suitable for SmoB: NADPH bound to SmoB with *K_d* ~2 μM, while no binding was observed for NADH (**Fig. S11, Table S3**). Thus, glucose pre-equilibrated in H₂¹⁸O was incubated with SmoB and NADP⁺ then analyzed by mass spectrometry to reveal the formation of a product 4 Da greater in mass than glucose, presumably due to the incorporation of two ¹⁸O atoms into glucose. The crude reaction mixture was subjected to peracetylation (Ac₂O/pyridine) then LC-MS analysis to confirm that the +4 Da product co-eluted with authentic D-glucose-pentaacetate (**Fig. S12**). To determine that the ¹⁸O label was being incorporated at C6 of glucose, we used electron-impact GC-MS, which required conversion of the reaction product to the acyclic pentapropionate aldonitrile (**Fig. S13**) (19). This approach provided diagnostic C1-C5 and C5-C6 fragment ions. The ¹⁸O-labelled product gave a C5-C6 fragment that was 2 mass units higher (*m/z* 173 versus 175), whereas the C1-C5 fragment was the same as unlabelled glucose reference (*m/z* 370), demonstrating that the ¹⁸O is incorporated at C6. Only enzymatic reactions conducted in the presence of NADP⁺ produced product labelled with ¹⁸O at C6: NAD⁺ failed to produce any product, supporting our observations by ITC and defining the cofactor specificity of SmoB.

We determined the 3D structure of SmoB using X-ray diffraction methods. This initial structure revealed that SmoB exists as a compact trimer, however the C-terminal His₆-tag in this construct occupied the putative active site of adjoining subunits, making co-crystallization with cofactors

difficult (**Fig. S14**). To overcome this issue, SmoB was subcloned into a different vector and expressed with a cleavable N-terminal purification tag. This protein maintained the same catalytic activity and SEC-MALS confirmed it remained a trimer in solution (**Fig. S15**). This SmoB construct was co-crystallized with NADPH and a ternary product complex obtained by soaking crystals with D-glucose (**Fig. 4b**). These crystals diffracted to a resolution of 1.5 Å and the resulting model revealed that SmoB is an (α/β)₈ TIM barrel fold with a C-terminal cofactor binding site. The overall fold has high structural conservation with members of the aldo-keto reductase (AKR) superfamily. SmoB binds NADPH with the 2'-phosphate oxygens hydrogen-bonded to Thr284, Arg289 and backbone amide of Asn285 and the adenine ring stacked between Arg289 and Phe241 at the C-terminus (**Fig. 4c**). NADPH binds in an extended *anti*-conformation and the nicotinamide ring is located at the base of the substrate binding pocket. Trp232 makes a π - π stacking interaction with the nicotinamide ring that positions the reactive center (C4) at a distance of 3 Å from C-6 of glucose, appropriate for hydride transfer (**Fig. 4d**). Within the SmoB•NADP⁺•glucose complex, glucose interacts with Arg152 (2.9 Å) and Lys120 (3 Å), as well as His151 (2.8 Å) and Tyr76 (2.7 Å) within the conserved catalytic tetrad His/Tyr/Lys/Asp that is common to the AKR superfamily (**Fig. 4e**) (20).

289

290 *SMO pathways occur in the Alphaproteobacteria and Betaproteobacteria*

To ascertain how widespread this pathway for SQ utilization might be, a Multigene BLAST search was conducted of the non-redundant protein set of the NCBI for gene clusters that contain homologous SQases and SQ monooxygenases. This identified many putative *smo* gene clusters across the *Agrobacterium* and *Rhizobium* genus within the *Rhizobiales* order and evidence of some broader expansion into the Alphaproteobacteria and Betaproteobacteria classes (**Fig. 5**). Amongst these putative *smo* gene clusters, some were syntenic while others were substantially rearranged (non-syntenic) or modified to make use of other (non-ABC) transporter systems. The use of diverse transport systems is not surprising: a similar phenomenon has been observed for the tier-1 sulfo-ED pathway (4, 5). Indeed, sulfo-ED gene clusters have been identified in several *Rhizobiales* (4, 5), suggesting that there has been ample opportunity for genetic exchanges between these pathways during their evolution.

301

Discussion

While existing pathways for the breakdown of SQ require two different organisms and involve scission of the carbon chain into two 3-carbon fragments, we describe here a fundamentally different approach that features complete utilization of the SQ carbon skeleton. The SMO pathway features several proteins with hitherto undescribed activities, including: an SQGro-binding protein; an FMNH₂- and O₂-dependent SQ monooxygenase that defines this ‘SMO’ pathway by catalyzing scission of the C–S bond in SQ; and an oxidoreductase dedicated to the NADPH-dependent reduction of 6-OG to glucose. Like all other sulfoglycolytic pathways studied to date, the SMO pathway also possesses a conserved SQase, which is essential for liberating SQ from its precursor glycoside SQGro (8, 9).

The SMO pathway is reminiscent of other sugar-metabolizing pathways in bacteria. For example, the SmoI (SQase), SmoF (SQGro binding protein) and SmoE/G/H (ABC transporter) proteins encoded by the *smo* cluster are analogous to MalP (maltodextrin phosphorylase), MalE (maltose binding protein) and MalF/G/K (ABC transporter) encoded by the *mal* operon of *E. coli* that imports and degrades maltose (21). Additionally, the SmoC (SQ monooxygenase) and SmoA (flavin reductase) proteins of the SMO pathway are reminiscent of the SsuD (FMNH₂-dependent alkylsulfonate monooxygenase) and SsuE (NADPH-dependent FMN reductase) pair encoded by the *ssu* operon of *E. coli* that degrades alkanesulfonates (15). Indeed, it is likely that the SMO pathway arose through the recombination and neofunctionalization of analogous sugar- and sulfonate-metabolising pathways.

Through structural analysis we identified key residues involved in sulfosugar recognition and processing, in order to provide greater confidence to bioinformatic analyses of putative *smo* gene clusters: an approach that has proven valuable for the identification of tier 1 sulfoglycolytic pathways (8, 22, 23). This includes the Thr220-Gly166-Ser43-H₂O(His13-Gln46) cluster of SmoF for the recognition of SQGro, the Arg283-Trp286-H₂O(Tyr491) triad of SmoI for the recognition of SQGro; and the Trp206-Arg236-His238-Tyr341-His343 constellation of SmoC for the recognition of SQ. Given the importance of the SQ monooxygenase SmoC to the SMO pathway, further empirical and computational work is warranted to understand what interactions drive its selectivity for SQ, which lies in contrast with the promiscuity exhibited by alkanesulfonate monooxygenases like SsuD.

The prevalence of the SMO pathway in Alphaproteobacteria of the *Rhizobiales* order is intriguing, since many bacteria of this order are plant symbionts or pathogens. Indeed, those bacteria that do not possess an SMO pathway often possess a complementary tier 1 sulfo-ED pathway (4). Accordingly,

337 it appears that plant sulfolipid catabolism is important for rhizobiales, whether they be plant
338 pathogens/symbionts or free-living organisms adopting an oligotrophic saprophytic lifestyle in
339 substrate replete with decaying plant tissues. Symbiotic bacteria of the *Rhizobiales* order reside within
340 the root nodules of their plant host, where they harness four-carbon substrates from the host for energy
341 and central metabolism (24). Sugawara and co-workers showed that sulfonate utilization gene clusters
342 were expressed by the plant symbiont *Bradyrhizobium diazoefficiens* USDA 110 within these nodules
343 and that this may be important for utilizing diverse sulfur sources to support symbiotic and possibly
344 free-living lifestyles (25). With sulfolipid representing a large and accessible pool of sulfur in plants,
345 one possible purpose of the SMO pathway may be to salvage sulfur for these bacteria. This is an
346 important distinction between the SMO pathway and the tier 1 sulfoglycolytic pathways: the latter
347 supports two-member microbial communities containing a second member with a tier 2 pathway to
348 provide access to the sulfur of SQ (26). In this sense, use of the SMO pathway, which enables the
349 complete utilization of the carbon skeleton and access to the sulfur of the monosaccharide can be
350 considered a ‘selfish’ metabolic strategy, and could provide an advantage in the highly competitive
351 soil environment or in the absence of other bacterial species within colonized plant tissues. Combined
352 with the pathway’s requirement for molecular oxygen to effect C–S bond fissure, this may explain
353 why the SMO pathway occurs within those bacteria that are commonly associated with plants.
354 Understanding how the SMO and tier 1 pathways impact fitness within different environmental
355 niches remains an important question, with answers that have significant implications for
356 understanding plant diseases and symbioses, as well as soil chemistry.

357

358 **Methods**

359 *Growth studies*

360 Cultures of *A. tumefaciens* C58 were grown in a phosphate-buffered mineral salts media (M9, pH
361 7.2), with glucose or SQ (10 mM) as the sole carbon source. Cultures were incubated at 30 °C (250
362 rpm), with adaptation and robust growth observed within 2–3 days. These were sub-cultured (1%
363 inoculum) into the same media (10 ml) and grown at 30 °C (250 rpm). Bacterial growth was
364 quantitated using a Varian Cary50 UV/visible spectrophotometer to measure OD₆₀₀. Growth
365 experiments were replicated twice.

367 *Reducing sugar assay for culture supernatant*

368 The reducing sugar assay was performed according to the procedure of Blakeney and Mutton(27).
369 This assay uses pre-prepared alkaline diluent and PAHBAH working solution. Alkaline diluent was
370 prepared by the addition of sodium hydroxide (20 g, 0.50 mol) to a solution of 0.10 M trisodium
371 citrate (50 mmol, 500 ml) and 0.02 M calcium chloride (13 mmol, 500 ml). PAHBAH working
372 solution was prepared by dissolving 4-hydroxybenzhydrazide (PAHBAH) (0.25 g, 1.6 mmol) in
373 alkaline diluent (50 ml). The PAHBAH working solution should be made fresh shortly before use.
374 To determine reducing sugar concentration, 0.90 ml of PAHBAH working solution was added to 0.10
375 ml of sample. The mixture was heated at 98 °C for 4 min then 0.5 ml of the mixture was diluted into
376 1.0 ml of deionized water and the absorbance read at 415 nm using a Varian Cary50 UV/visible
377 spectrophotometer. Concentrations of SQ were determined with reference to a standard curve
378 constructed using SQ.

380 *Turbidometric sulfate assay for culture supernatant*

381 The sulfate assay was performed according to the procedure of Sörbo (28). This assay uses a Ba-PEG
382 reagent, which contains PEG to stabilize BaSO₄ crystals and a small amount of pre-formed BaSO₄
383 seed crystals to improve the reproducibility and linearity of the assay. The Ba-PEG reagent should be
384 prepared fresh before use. Ba-PEG reagent was prepared by dissolving BaCl₂ (42 mg, 0.20 mmol)
385 and polyethylene glycol 6000 (0.75 g) in deionized water (5.0 ml). A small amount of Na₂SO₄ (10
386 µl, 50 mM) was added to this solution, with efficient magnetic stirring to generate preformed BaSO₄
387 seed crystals. Individual sulfate assays were conducted as follows. A sample (typically 100 µl,
388 containing a maximum of 2.5 µmol of Na₂SO₄) was diluted to 0.1 ml with deionized water before the
389 addition of 0.5 M HCl (0.1 ml) followed by Ba-PEG reagent (0.1 ml). The mixture was mixed
390 vigorously and the absorbance of the sample at 400 nm determined using a Varian Cary50 UV/visible
391 spectrophotometer. Concentrations of sulfate were determined by reference to a standard curve
392 constructed using Na₂SO₄.

393

394 *Colorimetric fuchsin sulfite assay for culture supernatant*

395 The fuchsin sulfite assay was performed according to the procedures of Brychkova *et al.* (29) and
396 Kurmanbayeva *et al.* (30). This procedure requires three pre-prepared solutions, Reagents A, B and
397 C. Reagent A was prepared by dissolution of basic fuchsin (4.0 mg, 12 μ mol) in deionized water
398 (8.25 ml) at 0 °C, prior to the addition of 98% H₂SO₄ (1.25 ml). Reagent B was prepared by diluting
399 formaldehyde (36% in H₂O, 0.32 ml) in deionized water (9.68 mL) at 0°C. Reagent C was prepared
400 by dilution of Reagent A (1 ml) in deionized water (7 ml), prior to the addition of solution reagent B
401 (1 ml). Individual sulfite assays were performed by addition of Reagent C (516 μ l) to a mixture of
402 sample (72 μ l) and 0.5 mM Na₂SO₃ (12 μ l), with the latter providing a stable background signal for
403 reference. The sample was incubated at r.t. for 10 min and the absorbance of the sample at 570 nm
404 determined using a Varian Cary50 UV/visible spectrophotometer. Concentrations of sulfite were
405 determined by reference to a standard curve constructed using Na₂SO₃.

406

407 *NMR analysis of metabolites produced from (¹³C₆)SQ*

408 M9 minimal media (5 ml) containing 10 mM glucose was inoculated with *A. tumefaciens* C58 and
409 grown to stationary phase at 30 °C (250 rpm). A 50 μ l aliquot of this culture was used to inoculate 2
410 ml of M9 minimal media containing 10 mM (¹³C₆)SQ and the culture incubated at 30 °C (250 rpm).
411 At OD₆₀₀ 0.27 and OD₆₀₀ 0.49, 950 μ l samples of culture supernatant were diluted with 100 μ l of D₂O
412 and ¹³C-NMR spectra acquired using a 400 MHz spectrophotomer (100 MHz for ¹³C).

413

414 *Growth of A. tumefaciens C58 on diverse alkanesulfonates*

415 M9 minimal media (5 ml) containing 10 mM glucose was inoculated with *A. tumefaciens* C58 and
416 grown to stationary phase at 30 °C (250 rpm). A 50 μ l aliquot of this starter culture was used to
417 inoculate 2 ml of M9 minimal media containing 10 mM of the alternative alkanesulfonate substrate:
418 SQ (positive control), methyl α -sulfoquinovoside (MeSQ), glycer-1-yl α -sulfoquinovoside (SQGro),
419 dicyclohexylammonium sulfolactate, cyclohexylammonium dihydroxypropanesulfonate, sulfoacetic
420 acid, taurine, sodium pentanesulfonate, cysteic acid, MOPS, HEPES, PIPES, MES and
421 methanesulfonic acid. Cultures were incubated for 30 days at 30 °C (250 rpm) with daily observations
422 of optical density at 600 nm. Each experiment was performed in duplicate. Growth was observed on
423 SQ (positive control), MeSQ, and SQGro, but not on any other sulfonate. Control experiments
424 established that *A. tumefaciens* grows on glucose in the presence and absence of cyclohexylamine or
425 dicyclohexylamine, and does not grow on cyclohexylamine or dicyclohexylamine alone.

426

427 *Digestion of samples for quantitative proteomics*

Freeze dried *A. tumefaciens* whole-cell pellets were resuspend in 500 µl lysis buffer (4% SDS, 50 mM Tris pH 8.5, 10 mM DTT) and boiled at 95 °C for 10 min with shaking at 2000 rpm to shear DNA and inactivate protease activity. Lysates were cooled to room temperature and protein concentration determined using a BCA assay. Each sample (200 µg of protein) was acetone precipitated by mixing 4 volumes of ice-cold acetone with one volume of sample. Samples were precipitated overnight at -20 °C and then centrifuged at 4000 × g for 10 min at 4 °C. The precipitated protein pellets were resuspended with 80% ice-cold acetone and precipitated for an additional 4 h at -20 °C. Samples were centrifuged at 17000 × g for 10 min at 4 °C to collect precipitated protein, the supernatant was discarded and excess acetone driven off at 65 °C for 5 min. Dried protein pellets were resuspended in 6 M urea, 2 M thiourea, 40 mM NH₄HCO₃ and reduced/alkylated prior to digestion with Lys-C (1/200 w/w) then trypsin (1/50 w/w) overnight as previously described (31). Digested samples were acidified to a final concentration of 0.5% formic acid and desalted using C18 stage tips (32) before analysis by LC-MS.

Quantitative proteomics using reversed phase LC-MS

Purified peptides were resuspended in Buffer A* (2% MeCN, 0.1% TFA) and separated using a Proflow-equipped Dionex Ultimate 3000 Ultra-Performance Liquid Chromatography system (Thermo Fisher Scientific) with a two-column chromatography set up composed of a PepMap100 C18 20 mm × 75 µm trap and a PepMap C18 500 mm × 75 µm analytical column (Thermo Fisher Scientific). Samples were concentrated onto the trap column at 5 µl min⁻¹ with Buffer A (2% MeCN, 0.1% FA) for 6 min and then infused into an Orbitrap Q-Exactive HF Mass Spectrometer (Thermo Fisher Scientific) at 250 nl min⁻¹. Peptides were separated using 124-min gradients altering the buffer composition from 2% Buffer B (80% MeCN, 0.1% FA) to 8% B over 14 min, then from 8% B to 30% B over 80 min, 30% B to 45% B over 10 min, 45% B to 95% B over 2 min, holding at 95% B for 10, then dropped to 2% B over 1 min and holding at 2% B for the remaining 7 min. The Q-Exactive HFTM Mass Spectrometer was operated in a data-dependent mode automatically switching between the acquisition of a single Orbitrap MS scan (120,000 resolution) and a maximum of 20 MS-MS scans (HCD NCE 28, maximum fill time 40 ms, AGC 2×10⁵ with a resolution of 15,000).

Mass spectrometry data analysis

Proteomics datasets were searched using MaxQuant (v1.5.3.3) (33) against the *A. tumefaciens* C58 proteome (Uniprot proteome id UP000000813, downloaded 27/01/2018, 5344 entries). Searches were performed with carbamidomethylation of cysteine set as a fixed modification and oxidation of methionine as well as acetylation of protein N-termini allowed as variable modifications. The protease specificity was set to trypsin allowing 2 miscleavage events with a maximum false discovery

rate (FDR) of 1.0% set for protein and peptide identifications. To enhance the identification of peptides between samples the Match Between Runs option was enabled with a precursor match window set to 2 min and an alignment window of 10 min. For label-free quantitation, the MaxLFQ option within Maxquant(34) was enabled in addition to the re-quantification module. The resulting protein group output was processed within the Perseus (v1.4.0.6) (35) analysis environment to remove reverse matches and common protein contaminants prior. For LFQ comparisons missing values were imputed using Perseus and Pearson correlations visualized using R. The mass spectrometry proteomics data have been deposited to the ProteomeXchange Consortium via the PRIDE (36) partner repository with the dataset identifier PXD014115.

Cloning

Oligonucleotides encoding Atu3277 (SmoA), Atu3278 (SmoB), Atu3279 (SmoC) and Atu3282 (SmoF) were amplified by PCR using Phusion polymerase HF master mix (NEB), the appropriate primers listed in **Table S1** and *A. tumefaciens* C58 gDNA as template. Oligonucleotides encoding RoSmoA and RoSmoC were synthesized (IDT) to provide the sequences listed in **Table S1**. These were cloned into the pET29b(+) vector at the *NdeI* and *XhoI* sites and sequence-verified by Sanger sequencing to give expression vectors for SmoA, SmoB, SmoC, SmoF, RoSmoA and RoSmoC. Due to interference from the SmoB C-terminal His₆-tag during structural studies, the *smoB* (Atu3278) gene was sub-cloned into the pET-YSBLIC3C vector (37) by PCR amplification with the relevant primers in **Table S1** and In-Fusion[®] cloning (Clontech Laboratories, Inc.) into linearized YSBLIC3C vector according to the manufacturer's protocol. The expression plasmid was sequence-verified by Sanger sequencing.

Protein expression and purification

All vectors were transformed into 'T7 Express' *E. coli* (NEB), except for the vector encoding SmoF (Atu3282), which was transformed into 'Shuffle[®] T7' *E. coli* (NEB), and all were plated onto LB-agar (50 µg/ml kanamycin) and incubated at 37 °C for 16 h. A single colony was used to inoculate 10 ml of LB media containing 50 µg/ml kanamycin and the cultures incubated at 37 °C for 16 h. These starter cultures were used to inoculate 1000 ml of S-broth (35 g tryptone, 20 g yeast extract, 5 g NaCl, pH 7.4) containing 50 µg/ml kanamycin, which was incubated with shaking (250 rpm) at 37 °C until it reached an OD₆₀₀ of 0.8. Each culture was cooled to room temperature, isopropyl thiogalactoside (IPTG) added to a final concentration of 400 µM, and incubation with shaking (200 rpm) continued at 18 °C for 19 h. Cells were harvested by centrifugation at 8,000 g for 20 min at 4 °C then resuspended in 40 ml binding buffer (50 mM NaPi, 300 mM NaCl, 5 mM imidazole, pH 7.5) containing protease inhibitor (Roche cOmplete EDTA-free protease inhibitor cocktail) and lysozyme

(0.1 mg/ml) by nutating at 4 °C for 30 min. Benzonase (1 µl) was added to the mixture then lysis was effected by sonication [10× (15 s on / 45 s off) at 45% amplitude]. The lysate was centrifuged at 18,000 g for 20 min at 4 °C and the supernatant collected. The supernatants were filtered (0.45 µm) and loaded onto a 1 ml HiTrap TALON IMAC column (GE). The column was washed with 3 × 10 ml of binding buffer, then the protein was eluted using elution buffer (50 mM NaPi, 300 mM NaCl, 400 mM imidazole, pH 7.5). Fractions containing product, as judged by SDS-PAGE, were further purified by size exclusion chromatography on a HiPrep 16/60 Sephacryl S-200 HR column (GE) using 50 mM NaPi, 150 mM NaCl, pH 7.5 (Atu3277 SmoA; Atu3278, SmoB; Atu3279, SmoC) or 50 mM sodium citrate, 150 mM NaCl, pH 5.5 (Atu3282, SmoF) as buffer (**Fig. S2**). SmoI (Atu3285 or AtSQase) was prepared as previously described (8).

SEC-MALS analyses

Experiments were conducted on a system comprising a Wyatt HELEOS-II multi-angle light scattering detector and a Wyatt rEX refractive index detector linked to a Shimadzu LC system (SPD-20A UV detector, LC20-AD isocratic pump system, DGU-20A3 degasser and SIL-20A autosampler). Experiments were conducted at room temperature (20 ± 2°C). Solvents were filtered through a 0.2 µm filter prior to use and a 0.1 µm filter was present in the flow path. The column was equilibrated with > 2 CV of buffer (50 mM NaPi, 300 mM NaCl pH 7.4) before use and buffer was infused at the working flow rate until baselines for UV, light scattering and refractive index detectors were all stable. The sample injection volume was 100 µl of protein at 6 mg ml⁻¹ in 50 mM NaPi buffer, 300 mM NaCl pH 7.4. Shimadzu LC Solutions software was used to control the LC and Astra V software for the HELEOS-II and rEX detectors. The Astra data collection was 1 min shorter than the LC solutions run to maintain synchronization. Blank buffer injections were used as appropriate to check for carry-over between sample runs. Data were analyzed using the Astra V software. Molecular weights were estimated using the Zimm fit method with degree 1. A value of 0.158 was used for protein refractive index increment (dn/dc).

Isothermal Titration Calorimetry

ITC experiments were performed using a MicroCal iTC200 (GE Healthcare) at 25 °C, with a 750 r.p.m. stirring speed and a reference power of 10 µCal.s⁻¹. Proteins and substrates were equilibrated into degassed and filter-sterilized buffer (50 mM NaPi, 200 mM NaCl, pH 7.4 for SmoC/F and 25 mM NaPi, pH 7.5 for Smo B). Protein concentration was determined by BCA assay (Thermo Fisher) before initiating experiments. For SmoC–SQ binding, 600 µM SQ was titrated into the ITC cell containing 40 µM SmoC as a series of 10 × 3.94 µl injections with a pre-injection of 1 × 0.4 µl. For SmoF–SQGro binding, 200 µM SQGro was titrated into the ITC cell containing 20 µM SmoF as a

533 series of $15 \times 2.94 \mu\text{l}$ injections with a pre-injection of $1 \times 0.4 \mu\text{l}$. The delay between injections was
534 set at 120 s, with an initial injection delay of 60 s. For SmoB-NAD(P)H binding, 1 mM NADH was
535 titrated into the ITC cell containing 40 μM SmoB as a series of $19 \times 3 \mu\text{l}$ injections with a pre-injection
536 of $1 \times 4 \mu\text{l}$. The delay between injections was set at 150 s, with an initial injection delay of 180 s. All
537 data analysis was performed in MicroCal ITC Origin Analysis software (Malvern).

538

539 *Nano Differential Scanning Fluorescence analysis of SmoF*

540 Thermal stability analysis for SmoF in the presence and absence of SQGro ligand was performed on
541 a Prometheus NT.48 (NanoTemper) at 15% excitation, scanning from 20 °C to 65 °C at 0.5 °C min⁻¹. All protein samples were at a concentration of 1 mg ml⁻¹ in 50 mM citrate, 150 mM NaCl at pH
542 5.5, with a 10 μl capillary load per sample. Data acquisition and analysis was performed with
543 PR.ThermControl (NanoTemper) software.

544

546 *Identification of the flavin co-factor that co-purified with SmoA*

547 100 μl of recombinant flavin reductase (SmoA or RoSmoA) at a concentration of 20 mg ml⁻¹ in 50
548 mM Tris, 150 mM NaCl, pH 8.5 was heated at 90 °C for 10 min. The sample was clarified by
549 centrifugation (16,000 $\times g$, 10 min, 4 °C) and the supernatant filtered (0.2 μm). Samples were analyzed
550 by LCMS on an Agilent LCMS system (G6125B mass detector, 1290 Infinity G7120A high speed
551 pump, 1290 Infinity G7129B autosampler, and 1290 Infinity G7117B diode array detector).
552 Conditions for LC were as follows: column: Phenomenex 00B-4752-AN Luna Omega 1.6 μm PS C₁₈
553 100Å (50 \times 2.1 mm); injection volume: 1 μl ; gradient: 3 to 100% B over 20 min (solvent A: water +
554 0.1% FA; solvent B: MeCN + 0.1% FA); flow rate: 0.6 ml/min; DAD – 254 and 214 nm.

555

556 *Michaelis-Menten kinetic analyses of SmoA and RoSmoA*

557 Reactions were conducted at 25 °C in 96-well plate format and involved the addition of SmoA or
558 RoSmoA (final concentration of 20 nM for NADH and 500 nM for NADPH) to 20–800 μM
559 NAD(P)H in 50 mM NaPi, 150 mM NaCl, 30 μM FMN, 0.01% BSA, pH 7.4 at a total volume of
560 100 μl . The progress of the enzyme-catalyzed conversion of NAD(P)H to NAD(P)⁺ was monitored
561 by measuring loss of absorbance at 340 nM over time using an Envision Multimodal Plate Reader
562 (Perkin Elmer). Initial rates for each reaction were calculated after first subtracting the rate of
563 spontaneous NAD(P)H oxidation (determined using an enzyme-free control) and an empirically
564 determined extinction coefficient for NAD(P)H under these conditions. Each initial rate was
565 determined in triplicate and fit to a Michaelis-Menten equation using Prism 8 (GraphPad).

566

567 *Sulfoquinovose monooxygenase assay*

568 This SQ monooxygenase activity assay is based on a previously described alkanesulfonate
569 monooxygenase activity assays (18) and uses Ellman's reagent to quantify sulfite released by these
570 enzymes. A 2 ml reaction containing 1 mM SQ, 1 mM NADH, 3 μ M FMN, 0.01% (w/v) BSA, 100
571 nM SmoA or RoSmoA and 300 nM SQ monooxygenase (SmoC or RoSmoC) in buffer (25 mM Tris
572 pH 9.1, 25 mM NaCl) was incubated at 30 °C, along with controls lacking reaction components or
573 using alternate sulfonate substrates. Reactions were initiated by the addition of SmoA or RoSmoA to
574 the mixture. Sulfite concentration in the samples was determined at discrete time points by quenching
575 40 μ l of the reaction in 160 μ l of Ellman's reagent (0.125 mg.ml⁻¹ in 25 mM NaPi pH 7.0, prepared
576 fresh) within a 96-well plate. After 60 s, the absorbance of the sample at 405 nm was determined
577 using an Envision Multimodal Plate Reader (Perkin Elmer). The sulfite concentration was
578 interpolated using a calibration curve generated under these conditions: a linear relationship between
579 sulfite concentration and absorbance at 405 nm was observed for 5–1000 μ M Na₂SO₃. The activity
580 of SQ monooxygenases at different pH was determined by modifying the buffer in the above reactions
581 (MES: pH 6.0, 6.5 and Tris: pH 7.0, 7.5, 8.0, 8.5, 9.1) using an endpoint of t = 30 min.

582

583 *Equilibrium isotope labelling using SmoB*

584 In order to pre-label the anomeric position, glucose was incubated in 98% H₂¹⁸O with heating at 80
585 °C for 2 days, then evaporated to dryness to give C1-¹⁸O-labelled glucose. Labelling was determined
586 to be 95% by mass spectrometry based on intensities of the M and M+2 peaks. Using H₂¹⁸O buffer
587 (100 mM potassium phosphate, pH 7.0), NAD⁺ and NADP⁺ were each added at 0.05 molar equivalent
588 to C1-¹⁸O-glucose and SmoB. Four control experiments were conducted: one without enzyme, one
589 without NAD⁺ and NADP⁺, one in H₂¹⁶O, and one in H₂¹⁶O with unlabeled glucose. Reactions were
590 monitored by mass spectrometry. Only in the experimental sample containing enzyme, H₂¹⁸O and
591 NAD⁺/NADP⁺ was an M+4 signal observed and this reached a maximum intensity after 72 h. Two
592 additional reactions were performed using SmoB, glucose and either NADP⁺ or NAD⁺ in H₂¹⁸O and
593 only the reaction containing NADP⁺ generated the M+4 species. To confirm that the M+4 species was
594 glucose with two ¹⁸O labels, we studied the product by HPLC. However, under aqueous HPLC
595 conditions the ¹⁸O-label at C1 is lost through chemical exchange with solvent. Therefore, we
596 acetylated the product to form the pentaacetate to ensure no exchange at the anomeric position during
597 HPLC analysis. The reaction mixture from above was evaporated under reduced pressure. The crude
598 residue was treated with acetic anhydride in pyridine (1:2, 1 ml) overnight. The product was extracted
599 with EtOAc and washed with sat. CuSO₄ to remove pyridine. The organic solution containing
600 peracetylated glucose was analyzed by LCMS on an Agilent LCMS system (G6125B mass detector,
601 1290 Infinity G7120A high speed pump, 1290 Infinity G7129B autosampler, and 1290 Infinity
602 G7117B diode array detector). Conditions for LC were as follows: column: Phenomenex 00B-4752-

603 AN Luna Omega 1.6 μm PS C_{18} 100Å (50×2.1 mm); injection volume: 1 μl ; gradient: 0 to 65% B
604 over 20 min (solvent A: water + 0.1% FA; solvent B: MeCN + 0.1% FA); flow rate: 0.6 ml/min. Peaks
605 with m/z 413 $[\text{M}+\text{Na}]^+$, m/z 415 $[\text{M}+2+\text{Na}]^+$, and m/z 417 $[\text{M}+4+\text{Na}]^+$ had the same retention time as
606 an authentic glucose pentaacetate standard.

607

608 *GC-MS analysis of isotopically-labelled carbohydrates*

609 A 0.1 μl aliquot of SmoB-glucose reaction mixture (containing ≈ 2.5 nmol glucose) was transferred
610 to a GC vial insert (deactivated) together with 1 nmol *scyllo*-inositol as an internal standard. Samples
611 were derivatized as described in Antoniewicz *et al.* (19), with minor modifications. Briefly, samples
612 were dried (*in vacuo*, 35 °C with a 40 μl methanol wash), followed by addition of hydroxylamine
613 hydrochloride (20 mg ml^{-1} in 25 μl pyridine) and incubation at 90 °C for 1 h. Vials were cooled briefly
614 at r.t. before the addition of propionic anhydride (50 μl) and incubation at 60 °C for 30 min. Samples
615 were evaporated to dryness under a stream of nitrogen at 60 °C and resuspended in EtOAc (40 μl).
616 Control samples of U- ^{12}C -glucose, U- ^{13}C -glucose, 1,2- $^{13}\text{C}_2$ -glucose and 6,6- $^2\text{H}_2$ -glucose were also
617 prepared at a 2.5 nmol scale in the assay buffer mixture. Samples were blinded for analysis. The
618 derivatized labelled glucose samples (**Fig. S13** and **Table S7**) were analyzed by GC-MS using a DB5
619 capillary column (J&W Scientific, 30 m, 250 μm inner diameter, 0.25 μm film thickness) with a 10
620 m inert duraguard. The injector insert and GC-MS transfer line temperatures were 270 °C and 250
621 °C, respectively. The oven temperature gradient was programmed as follows: 70 °C (1 min); 70 °C
622 to 295 °C at 12.5 °C min^{-1} ; 295 °C to 320 °C at 25 °C min^{-1} ; 320 °C for 2 min. Glucose and *scyllo*-
623 inositol were identified by reference to authentic standards. A calibration curve was generated using
624 glucose standard in assay buffer (starting concentration 50 nmol, 2-fold dilution series). **Fig. S12**
625 shows the fraction of labelled fragments, corrected for isotope natural abundance by DExSI analysis
626 (38).

627

628 *Protein crystallization*

629 Initial crystallization screening was performed using commercially available INDEX (Hampton
630 Research), PACT premier and CSSI/II (Molecular Dimensions) screens in 96-well sitting drop trays.
631 Further optimization was carried out in a 48-well sitting drop or 24-well hanging-drop format to
632 obtain optimal crystals for X-ray diffraction. Unless otherwise stated, all crystals were grown at 20
633 °C.

634

635 Crystals of apo-SmoF were obtained by mixing 0.15 μl of protein stock (50 mg ml^{-1} protein in 50
636 mM citrate, 150 mM NaCl, pH 5.5) with 0.15 μl mother liquor (0.3 M ammonium acetate, 0.1 M Bis-
637 Tris, 25% w/v PEG 3350, pH 5.5) housed in a Rigaku Xtaltrak plate hotel to enable consistent growth

638 and monitoring at 6 °C. Crystals were harvested with nylon CryoLoopsTM (Hampton Research) and
639 cryopreserved in liquid nitrogen without additional cryoprotectants.

640

641 Crystals of SmoF were initially obtained by mixing 0.15 µl of protein stock (3.5 mg ml⁻¹ protein with
642 2'R-SQGro at a 1:10 molar ratio in 50 mM citrate, 150 mM NaCl, pH 5.5) with 0.15 µl mother liquor
643 (30% (w/v) polyethylene glycol 4000, 0.2 M sodium acetate, 0.1 M tris chloride, pH 8.5). The
644 resulting crystals were used to prepare a seed stock by mixing the crystallization drop with 100 µl
645 mother liquor and vortexing for 60 s with one teflon bead. An optimisation plate was setup with drops
646 comprised of 0.1 µl of various mother liquors (28-36% (w/v) polyethylene glycol 4000, 0.2 M sodium
647 acetate, 0.1 M tris chloride, pH 7.1-9.1), 50 nl seed stock solution, and 0.15 µl protein stock (4 mg
648 ml⁻¹ protein with 2'R-SQGro at a 1:10 molar ratio in 50 mM citrate, 150 mM NaCl, pH 5.5). A single
649 crystal grown at 31.8% (w/v) polyethylene glycol 4000, 0.2 M sodium acetate, 0.1 M tris chloride,
650 pH 8.95, was harvested with a nylon CryoLoopTM (Hampton Research) and cryopreserved in liquid
651 nitrogen with 25% (v/v) ethylene glycol as cryoprotectant.

652

653 Crystals of SmoI-D455N-E370A-E371A were obtained by mixing 0.4 µl of protein stock (35 mg ml⁻¹
654 ¹ protein in 50 mM NaPi, 300 mM NaCl, pH 7.4) with 0.5 µl mother liquor (26% PEG 3350 w/v, 0.2
655 M KSCN, 0.1 M Bis-Tris propane, pH 6.5). Crystals were soaked with solid SQGro in mother liquor
656 for 2 min prior to harvesting with nylon CryoLoopsTM (Hampton Research) and cryopreserved
657 without additional cryoprotectants.

658

659 Crystals of apo-SmoC were obtained by mixing 0.6 µl of protein stock (60 mg ml⁻¹ protein in 50 mM
660 Tris, 300 mM NaCl, pH 7.5) with 0.5 µl mother liquor (0.2 M NaCl, 0.1 M MES pH 6, 26% PEG
661 6000 w/v and 10 mM SQ-glucitol). Crystals of apo-RoSmoC were obtained by mixing 0.1 µl of
662 protein stock (11.7 mg ml⁻¹ protein in 50 mM Tris, 300 mM NaCl, pH 7.5) with 0.2 µl mother liquor
663 (0.2M NaNO₃, 20% PEG 3350 w/v and 10 mM SQ). Crystals were harvested with nylon
664 CryoLoopsTM (Hampton Research) and cryopreserved in liquid nitrogen without additional
665 cryoprotectants.

666

667 Crystals of SmoB-apo (YSBLIC3C construct) were obtained by mixing 0.15 µl of protein stock (20
668 mg ml⁻¹ protein in 50 mM NaPi, 150 mM NaCl, pH 7.4) with 0.15 µl mother liquor (0.2 M sodium
669 malonate dibasic monohydrate, 0.1 M Bis-Tris propane pH 8.5, 20% w/v PEG 3350). For the
670 SmoB•NADPH complex, crystals were obtained by mixing 0.15 µl of protein stock (20 mg ml⁻¹
671 protein in 50 mM NaPi, 150 mM NaCl, 2 mM NADPH, pH 7.4) with 0.15 µl mother liquor (0.1 M
672 succinic acid, sodium dihydrogen phosphate, glycine buffer (SPG buffer, Qiagen), 25% w/v PEG

1500 at pH 6.0). For the SmoB•NADPH•Glc complex, crystals were obtained in a hanging drop by mixing 1 µl of protein stock (13 mg ml⁻¹ protein in 50 mM NaPi 150 mM NaCl, pH 7.4) with 1 µl of mother liquor (2 mM NADPH, 0.1 M SPG (Qiagen), 25% w/v PEG 1500 at pH 6). Crystals were soaked with solid glucose in mother liquor for 1 min prior to harvesting with nylon CryoLoops™ (Hampton Research) and cryopreserved without additional cryoprotectants.

X-ray data collection, processing and refinement

The data were processed and integrated using XDS (39) and scaled using SCALA (40) included in the Xia2 processing system (41). Data reduction was performed with AIMLESS, and resolution was cut until CC1/2 = 0.5. The structure of the SmoI•SQGro complex was determined using molecular replacement using 5OHS (8) as the initial model. For SmoF, the structure was solved by molecular replacement using PHASER (42) with a search model created from PDB ID: 6DTQ (43). The structure of RoSmoC was solved by molecular replacement using the ensemble based on PDB ID: 1M41 (18) as an initial search model. The structure of SmoB was determined using molecular replacement with the monomer of an aldo-keto reductase from *S. enterica* (PDB ID: 4R9O) as the initial model. The apo-SmoF structure was solved using a dissected C-terminal domain of the SmoF•SQGro structure. Structures were built and refined by iterative cycles using Coot (44) and REFMAC (45) or Phenix (46), the latter employing local NCS restraints. Following building and refinement of the protein and water molecules, clear residual density was observed in the omit maps for co-complex structures, respective ligands were modelled into these. The coordinate and refinement library files were prepared using ACEDRG (47). The final structures gave R_{cryst} and R_{free} values along with data and refinement statistics that are presented in **Table S4-6**. Data were collected at Diamond light source, Didcot, Oxfordshire, U.K., on beamlines I24 (SmoI-D455N•SQGro, to 2.15 Å; SmoF-apo, to 1.88 Å), I04 (RoSmoC to 1.75 Å) and I04-1 (SmoC-apo, to 3.2 Å; SmoB-apo_YSBLIC3C, to 1.5 Å; SmoB-apo; pET29a; SmoB•NADPH and SmoB•NADPH•Glc) and at the Australian Synchrotron using the MX2 beamline (At3282•SQGro complex, to 1.7 Å). The coordinate files and structure factors have been deposited in the Protein DataBank (PDB) with the coordinate accession numbers 7OFX (SmoI-D455N•SQGro), 7NBZ (SmoF-apo), 7OFY (SmoF•SQGro), 7OH2 (RoSmoC), 7OLF (SmoC-apo), 7BBY (SmoB-apo; pET29a), 7BBZ (SmoB-apo; YSBLIC3C), 7BC0 (SmoB•NADPH) and 7BC1 (SmoB•NADPH•Glc).

Structure-based analyses

Crystal packing interactions were analyzed using the protein interactions, surfaces, and assemblies (PISA) server (48). Structural comparisons and structure-based sequence alignments were conducted

707 using PDB25 search on DALI server against a representative subset of the Protein Data Bank (49).
708 All structure figures were generated using ccp4mg (50).

709

710 *Bioinformatic analysis SMO pathway prevalence*

711 Each gene within the *A. tumefaciens* C58 SMO gene cluster (*Atu3277-Atu3285*) was submitted as a
712 query to the NCBI BLASTp algorithm to search a database comprised of non-redundant protein
713 sequences with *A. tumefaciens* (taxid: 358) sequences excluded. Standard algorithm parameters were
714 used, except the maximum target sequences was set to 10,000. Results were filtered to only retain
715 protein sequences with E-value $\leq 1.19 \times 10^{-51}$. The corresponding nucleotide accession numbers for
716 each protein from all nine searches were extracted, combined and duplicates removed to provide a
717 list of candidate genome sequences. This was converted into a reference library for MultiGeneBLAST
718 (51) and queried using the *A. tumefaciens* C58 SMO gene cluster. Clusters identified by this workflow
719 with both an SQ monooxygenase and SQase homolog were regarded as putative SMO gene clusters.
720 Clusters representative of the observed diversity were visualized using Clinker (52). A phylogenetic
721 tree of species possessing a putative SMO gene cluster was generated by pruning the All-Species
722 Living Tree Project's 16s rRNA release 132 (53) using iTOL (54).

723

724 **Data Availability Statement**

725 All relevant data are available from the authors upon request. Structure coordinates have been
726 deposited in the Protein Data Bank (<https://www.rcsb.org/>) under accession codes 7OFX, 7OFY,
727 7NBZ, 7OH2, 7OLF, 7BBZ, 7BC0, 7BC1 and 7BBY. Proteomics data are available via
728 ProteomeXchange (55) (<http://www.proteomexchange.org/>) with the identifier PXD014115.

729

- 731 1. E. D. Goddard-Borger, S. J. Williams Sulfoquinovose in the biosphere: occurrence,
732 metabolism and functions. *Biochem. J.* **474**, 827–849 (2017).
- 733 2. J. L. Harwood, R. G. Nicholls The plant sulfolipid - a major component of the sulphur
734 cycle. *Biochem. Soc. Trans.* **7**, 440-447 (1979).
- 735 3. K. Denger, *et al.* Sulphoglycolysis in *Escherichia coli* K-12 closes a gap in the
736 biogeochemical sulphur cycle. *Nature* **507**, 114-117 (2014).
- 737 4. A. K. Felux, D. Spiteller, J. Klebensberger, D. Schleheck Entner-Doudoroff pathway for
738 sulfoquinovose degradation in *Pseudomonas putida* SQ1. *Proc. Natl. Acad. Sci. USA* **112**,
739 E4298-4305 (2015).
- 740 5. J. Li, *et al.* A Sulfoglycolytic Entner-Doudoroff Pathway in *Rhizobium leguminosarum* bv.
741 *trifolii* SRDI565. *Appl. Environ. Microbiol.* **86**, e00750-00720 (2020).
- 742 6. B. Frommeyer, *et al.* Environmental and Intestinal Phylum Firmicutes Bacteria Metabolize
743 the Plant Sugar Sulfoquinovose via a 6-Deoxy-6-sulfofructose Transaldolase Pathway.
744 *iScience* **23**, 101510 (2020).
- 745 7. Y. Liu, *et al.* A transaldolase-dependent sulfoglycolysis pathway in *Bacillus megaterium*
746 DSM 1804. *Biochem. Biophys. Res. Commun.* **533**, 1109-1114 (2020).
- 747 8. P. Abayakoon, *et al.* Structural and Biochemical Insights into the Function and Evolution of
748 Sulfoquinovosidases. *ACS Cent. Sci.* **4**, 1266-1273 (2018).
- 749 9. G. Speciale, Y. Jin, G. J. Davies, S. J. Williams, E. D. Goddard-Borger YihQ is a
750 sulfoquinovosidase that cleaves sulfoquinovosyl diacylglyceride sulfolipids. *Nat. Chem.*
751 *Biol.* **12**, 215-217 (2016).
- 752 10. A. B. Roy, M. J. Hewlins, A. J. Ellis, J. L. Harwood, G. F. White Glycolytic breakdown of
753 sulfoquinovose in bacteria: a missing link in the sulfur cycle. *Appl. Environ. Microbiol.* **69**,
754 6434-6441 (2003).
- 755 11. M. A. Kertesz Riding the sulfur cycle - metabolism of sulfonates and sulfate esters in Gram-
756 negative bacteria. *FEMS Microbiol. Rev.* **24**, 135-175 (2000).
- 757 12. P. Abayakoon, *et al.* Comprehensive synthesis of substrates, intermediates and products of
758 the sulfoglycolytic Embden-Meyerhoff-Parnas pathway. *J. Org. Chem.* **84**, 2910-2910
759 (2019).
- 760 13. A. E. Speers, C. C. Wu Proteomics of Integral Membrane Proteins: Theory and Application.
761 *Chem. Rev.* **107**, 3687-3714 (2007).
- 762 14. A. L. Davidson, E. Dassa, C. Orelle, J. Chen Structure, Function, and Evolution of Bacterial
763 ATP-Binding Cassette Systems. *Microbiol. Mol. Biol. Rev.* **72**, 317-364 (2008).
- 764 15. J. R. van Der Ploeg, R. Iwanicka-Nowicka, T. Bykowski, M. M. Hryniewicz, T. Leisinger
765 The *Escherichia coli* ssuEADCB gene cluster is required for the utilization of sulfur from
766 aliphatic sulfonates and is regulated by the transcriptional activator Cbl. *J. Biol. Chem.* **274**,
767 29358-29365 (1999).
- 768 16. A. Thakur, *et al.* Substrate-Dependent Mobile Loop Conformational Changes in
769 Alkanesulfonate Monooxygenase from Accelerated Molecular Dynamics. *Biochemistry* **59**,
770 3582-3593 (2020).
- 771 17. J. J. M. Liew, I. M. El Saudi, S. V. Nguyen, D. K. Wicht, D. P. Dowling Structures of the
772 alkanesulfonate monooxygenase MsuD provide insight into C-S bond cleavage, substrate
773 scope, and an unexpected role for the tetramer. *J. Biol. Chem.* **297**, (2021).
- 774 18. E. Eichhorn, C. A. Davey, D. F. Sargent, T. Leisinger, T. J. Richmond Crystal Structure of
775 *Escherichia coli* Alkanesulfonate Monooxygenase SsuD. *J. Mol. Biol.* **324**, 457-468 (2002).
- 776 19. M. R. Antoniewicz, J. K. Kelleher, G. Stephanopoulos Measuring deuterium enrichment of
777 glucose hydrogen atoms by gas chromatography/mass spectrometry. *Anal. Chem.* **83**, 3211-
778 3216 (2011).
- 779 20. T. M. Penning The aldo-keto reductases (AKRs): Overview. *Chem. Biol. Interact.* **234**, 236-
780 246 (2015).

- 781 21. R. Dippel, W. Boos The Maltodextrin System of *Escherichia coli*: Metabolism and
782 Transport. *J. Bacteriol.* **187**, 8322 (2005).
- 783 22. M. Sharma, *et al.* Dynamic Structural Changes Accompany the Production of
784 Dihydroxypropanesulfonate by Sulfolactaldehyde Reductase. *ACS Catalysis* **10**, 2826-2836
785 (2020).
- 786 23. M. Sharma, *et al.* Molecular Basis of Sulfosugar Selectivity in Sulfoglycolysis. *ACS Cent.*
787 *Sci.* **7**, 476-487 (2021).
- 788 24. M. Udvardi, P. S. Poole Transport and metabolism in legume-rhizobia symbioses. *Annu.*
789 *Rev. Plant Biol.* **64**, 781-805 (2013).
- 790 25. J. J. Speck, E. K. James, M. Sugawara, M. J. Sadowsky, P. Gyaneshwar An Alkane
791 Sulfonate Monooxygenase Is Required for Symbiotic Nitrogen Fixation by *Bradyrhizobium*
792 *diazoefficiens* (syn. *Bradyrhizobium japonicum*) USDA110(T). *Appl. Environ. Microbiol.*
793 **85**, (2019).
- 794 26. K. Denger, T. Huhn, K. Hollemeyer, D. Schleheck, A. M. Cook Sulfoquinovose degraded
795 by pure cultures of bacteria with release of C₃-organosulfonates: complete degradation in
796 two-member communities. *FEMS Microbiol. Lett.* **328**, 39-45 (2012).
- 797 27. A. B. Blakeney, L. L. Mutton A simple colorimetric method for the determination of sugars
798 in fruit and vegetables. *J. Sci. Food Agric.* **31**, 889-897 (1980).
- 799 28. B. Sörbo (1987) Sulfate: Turbidimetric and nephelometric methods. *Methods Enzymol.*,
800 (Academic Press), Vol 143, pp 3-6.
- 801 29. G. Brychkova, D. Yarmolinsky, R. Fluhr, M. Sagi The determination of sulfite levels and its
802 oxidation in plant leaves. *Plant Sci.* **190**, 123-130 (2012).
- 803 30. A. Kurmanbayeva, *et al.* (2017) Determination of Total Sulfur, Sulfate, Sulfite, Thiosulfate,
804 and Sulfolipids in Plants. *Plant Stress Tolerance: Methods and Protocols*, ed Sunkar R
805 (Springer New York, New York, NY), pp 253-271.
- 806 31. N. E. Scott, *et al.* Simultaneous glycan-peptide characterization using hydrophilic
807 interaction chromatography and parallel fragmentation by CID, higher energy collisional
808 dissociation, and electron transfer dissociation MS applied to the N-linked glycoproteome of
809 *Campylobacter jejuni*. *Mol. Cell. Proteomics* **10**, M000031-mcp000201 (2011).
- 810 32. J. Rappsilber, M. Mann, Y. Ishihama Protocol for micro-purification, enrichment, pre-
811 fractionation and storage of peptides for proteomics using StageTips. *Nat. Protoc.* **2**, 1896-
812 1906 (2007).
- 813 33. J. Cox, M. Mann MaxQuant enables high peptide identification rates, individualized p.p.b.-
814 range mass accuracies and proteome-wide protein quantification. *Nat. Biotechnol.* **26**, 1367-
815 1372 (2008).
- 816 34. J. Cox, *et al.* Accurate Proteome-wide Label-free Quantification by Delayed Normalization
817 and Maximal Peptide Ratio Extraction, Termed MaxLFQ. *Mol. Cell. Proteomics* **13**, 2513
818 (2014).
- 819 35. S. Tyanova, *et al.* Visualization of LC-MS/MS proteomics data in MaxQuant. *Proteomics*
820 **15**, 1453-1456 (2015).
- 821 36. Y. Perez-Riverol, *et al.* The PRIDE database and related tools and resources in 2019:
822 improving support for quantification data. *Nucleic Acids Res.* **47**, D442-d450 (2019).
- 823 37. Mark J. Fogg, Anthony J. Wilkinson Higher-throughput approaches to crystallization and
824 crystal structure determination. *Biochem. Soc. Trans.* **36**, 771-775 (2008).
- 825 38. M. J. Dagley, M. J. McConville DExSI: a new tool for the rapid quantitation of ¹³C-labelled
826 metabolites detected by GC-MS. *Bioinformatics (Oxford, England)* **34**, 1957-1958 (2018).
- 827 39. W. Kabsch Xds. *Acta Crystallogr., Section D: Biol. Crystallogr.* **66**, 125-132 (2010).
- 828 40. P. Evans Scaling and assessment of data quality. *Acta Crystallogr. Sect. D* **62**, 72-82 (2006).
- 829 41. G. Winter xia2: an expert system for macromolecular crystallography data reduction. *J.*
830 *Appl. Crystallogr.* **43**, 186-190 (2010).
- 831 42. L. C. Storoni, A. J. McCoy, R. J. Read Likelihood-enhanced fast rotation functions. *Acta*
832 *Crystallogr. D Biol. Crystallogr.* **60**, 432-438 (2004).

- 833 43. S. Shukla, *et al.* Differential Substrate Recognition by Maltose Binding Proteins Influenced
834 by Structure and Dynamics. *Biochemistry* **57**, 5864-5876 (2018).
- 835 44. P. Emsley, K. Cowtan Coot: Model-building tools for molecular graphics. *Acta Crystallogr.,*
836 *Sect. D: Biol. Crystallogr.* **60**, 2126-2132 (2004).
- 837 45. G. N. Murshudov, A. A. Vagin, E. J. Dodson Refinement of Macromolecular Structures by
838 the Maximum-Likelihood Method. *Acta Crystallogr. Sect. D* **53**, 240-255 (1997).
- 839 46. P. D. Adams, *et al.* PHENIX: a comprehensive Python-based system for macromolecular
840 structure solution. *Acta Crystallogr. D Biol. Crystallogr.* **66**, 213-221 (2010).
- 841 47. F. Long, *et al.* AceDRG: a stereochemical description generator for ligands. *Acta*
842 *Crystallogr. Sect. D* **73**, 112-122 (2017).
- 843 48. E. Krissinel, K. Henrick Secondary-structure matching (SSM), a new tool for fast protein
844 structure alignment in three dimensions. *Acta Crystallogr. D* **60**, 2256-2268 (2004).
- 845 49. L. Holm, P. Rosenström Dali server: conservation mapping in 3D. *Nucleic Acids Res.* **38**,
846 W545-W549 (2010).
- 847 50. S. McNicholas, E. Potterton, K. S. Wilson, M. E. M. Noble Presenting your structures: the
848 CCP4mg molecular-graphics software. *Acta Crystallogr. D* **67**, 386-394 (2011).
- 849 51. M. H. Medema, E. Takano, R. Breitling Detecting sequence homology at the gene cluster
850 level with MultiGeneBlast. *Mol. Biol. Evol.* **30**, 1218-1223 (2013).
- 851 52. C. L. M. Gilchrist, Y. H. Chooi Clinker & clustermap.js: Automatic generation of gene
852 cluster comparison figures. *Bioinformatics (Oxford, England)*, (2021).
- 853 53. P. Yilmaz, *et al.* The SILVA and “All-species Living Tree Project (LTP)” taxonomic
854 frameworks. *Nucl. Acids Res.* **42**, D643-D648 (2013).
- 855 54. I. Letunic, P. Bork Interactive Tree Of Life (iTOL) v4: recent updates and new
856 developments. *Nucl. Acids Res.* **47**, W256-W259 (2019).
- 857 55. E. W. Deutsch, *et al.* The ProteomeXchange consortium in 2017: supporting the cultural
858 change in proteomics public data deposition. *Nucl. Acids Res.* **45**, D1100-D1106 (2016).

859

860

Acknowledgements

Dr Monica Doblin is thanked for the provision of *Agrobacterium tumefaciens* strain C58. This work was supported in part by National Health and Medical Research Council of Australia (NHMRC) project grants GNT1100164 (N.E.S), GNT1174405 (D.B.A.), GNT1139546 and GNT1139549 (E.D.G.-B); the Leverhulme Trust grant RPG-2017-190 (G.J.D.); Australian Research Council grant DP180101957 and DP210100233 (S.J.W.), and DP210100362 (N.E.S.); and support from The Walter and Eliza Hall Institute of Medical Research, the Australian Cancer Research Fund and a Victorian State Government Operational Infrastructure support grant (E.D.G.-B). G.J.D is supported by the Royal Society Ken Murray Research Professorship, E.D.G.-B. is supported by the Brian M. Davis Charitable Foundation Centenary Fellowship, M.J.M. is an NHMRC Principal Research Fellow, N.E.S. is supported by and Australian Research Council Future Fellowship (FT200100270), B.M. was supported by Melbourne Research Scholarship, J.M. by a Sir John and Lady Higgins Scholarship, M.P. by an Australian Postgraduate Award. We acknowledge Dr. Johan P. Turkenburg and Sam Hart for assistance with X-ray data collection; the Diamond Light Source for access to beamlines I04, i24 and I04-1 under proposal number mx-18598; and the Australian Synchrotron, part of ANSTO, for access to the MX-2 beamline, which made use of the Australian Cancer Research Foundation (ACRF) detector. We thank the 'Melbourne Mass Spectrometry and Proteomics Facility' of the Bio21 Molecular Science and Biotechnology Institute at The University of Melbourne for the support of mass spectrometry analysis and the 'Bioscience Technology Facility' (University of York) for assistance with SEC-MALS analyses.

Author Contributions

EDG-B discovered the SMO gene cluster; SJW, EDG-B, GJD conceived project; MP and JW-YM conducted microbial growth experiments; NES conducted proteomics; JPL, MS, AS, MJ performed molecular biology, protein expression and structural and biophysical characterization; YZ, JPL, AS, MS, RM performed biochemical assays; ECS and MJM conducted carbohydrate analysis; YZ, JW-YM, BM and DA performed bioinformatics analysis; SJW, MS, EGB wrote the paper with input from all authors.

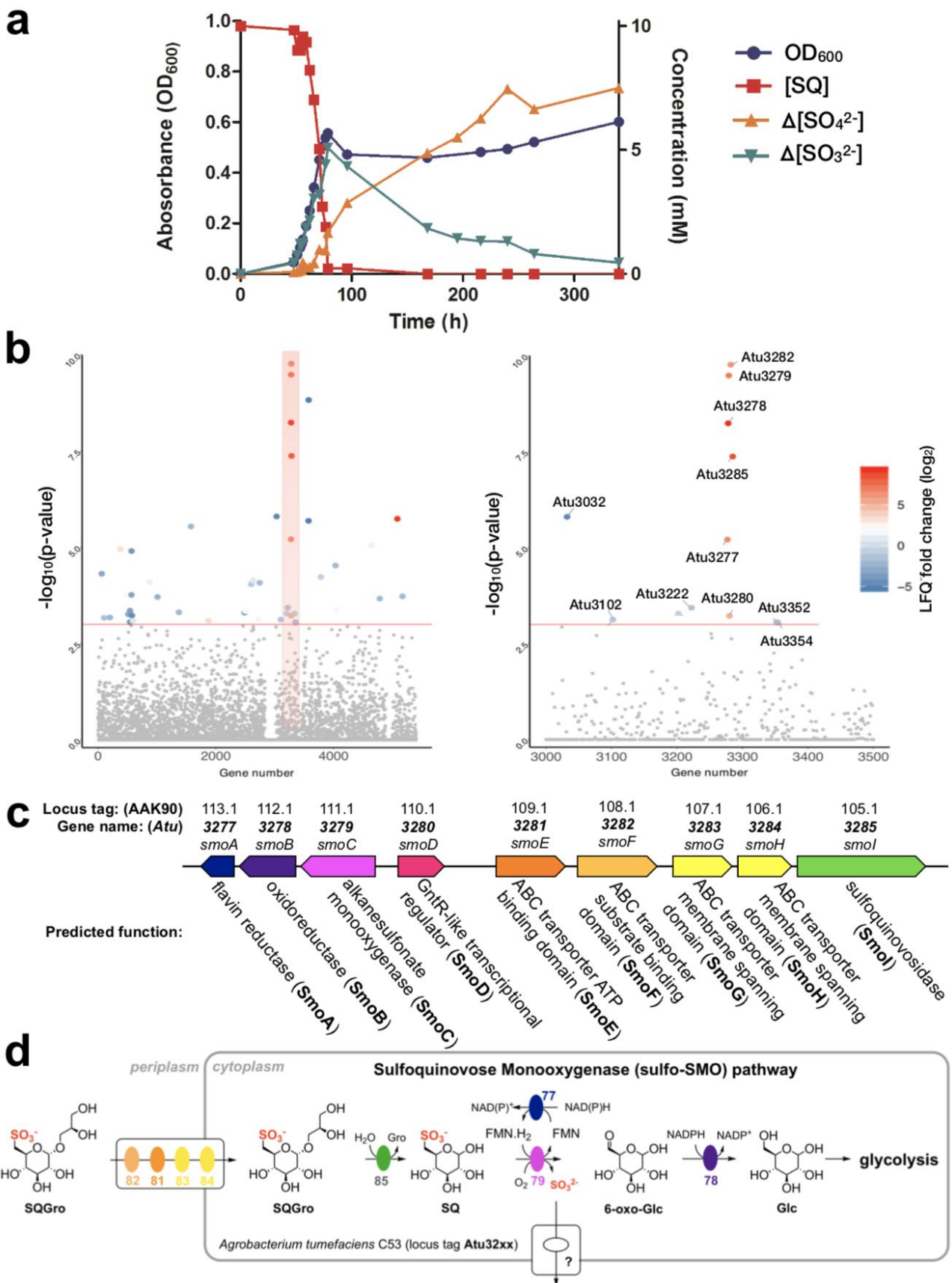
Competing Financial Interests Statement

The authors declare no competing interests.

Additional information

Supplementary information

Correspondence and requests for materials should be addressed to S.J.W, G.J.D or E.D.G.-B.



897

898

899

900

Figure 1: *A. tumefaciens* utilizes SQ and its glycosides as a carbon source. (a) Optical density of *A. tumefaciens* C58 culture (blue) and [SQ] (red), change in [sulfite] (green) and change in [sulfate] (yellow), with respect to time. (b) Manhattan plot of comparative proteomics data for *A. tumefaciens*

901 C58 grown on SQ vs glucose, demonstrating that the most heavily upregulated proteins belong to a
902 single gene cluster. (c) A cartoon of the upregulated cluster with automated annotations for each of
903 the gene products. These would later be renamed *smoABCDEFGHI*, to reflect the importance of the
904 sulfoquinovose monooxygenase enzyme activity to this new biochemical pathway. (d) A cartoon
905 illustrating the hypothetical roles played by the gene products of this pathway to complete the
906 catabolism of SQGro.

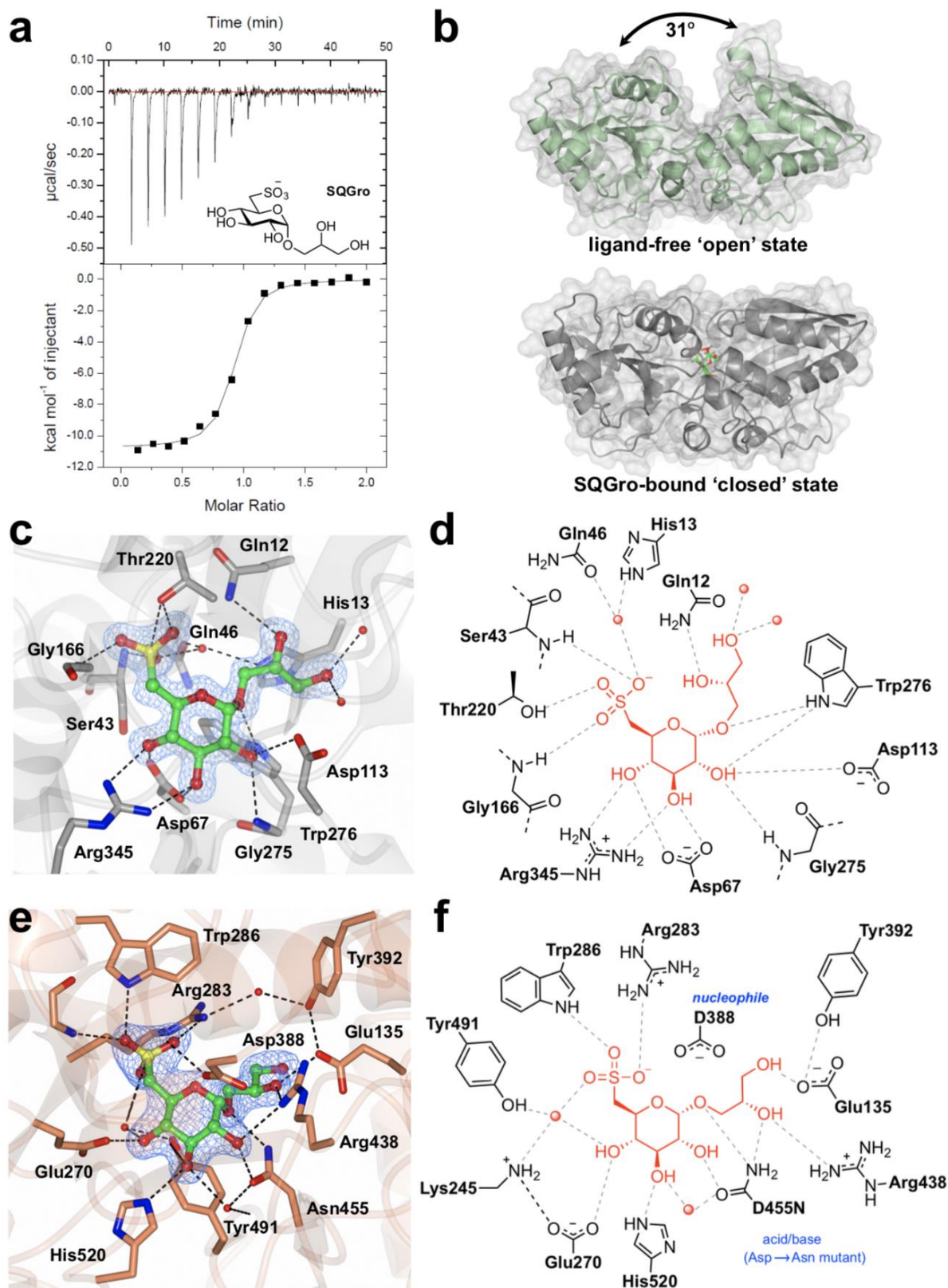


Figure 2: Biochemical and structural analyses of the SQGro-binding protein SmoF (Atu3282) and SQase SmoI (Atu3285). (a) A representative ITC isotherm for SmoF titrated against its cognate ligand 2'R-SQGro. (b) Ribbon diagrams (with transparent surface) for the open and closed (liganded) conformations of SmoF. 2'R-SQGro is bound tightly in the inter-domain cleft and is inaccessible to the bulk solvent in the closed conformation. (c) Interactions between protein and ligand within the

913 SmoF•2'*R*-SQGro complex: SmoF is in grey, 2'*R*-SQGro is in green, and the 2Fo – Fc map at 1.5σ
914 is in blue. (d) A cartoon highlighting key interactions from c. (e) Interactions between protein and
915 ligand within the complex pf SmoI-D455N SQase and 2'*R*-SQGro: SmoI is in gold, 2'*R*-SQGro is in
916 green, and the 2Fo – Fc map at 1.5σ is in blue. (f) A cartoon highlighting key interactions from e: red
917 spheres represent ordered water molecules; dotted lines represent proposed hydrogen bonds.
918

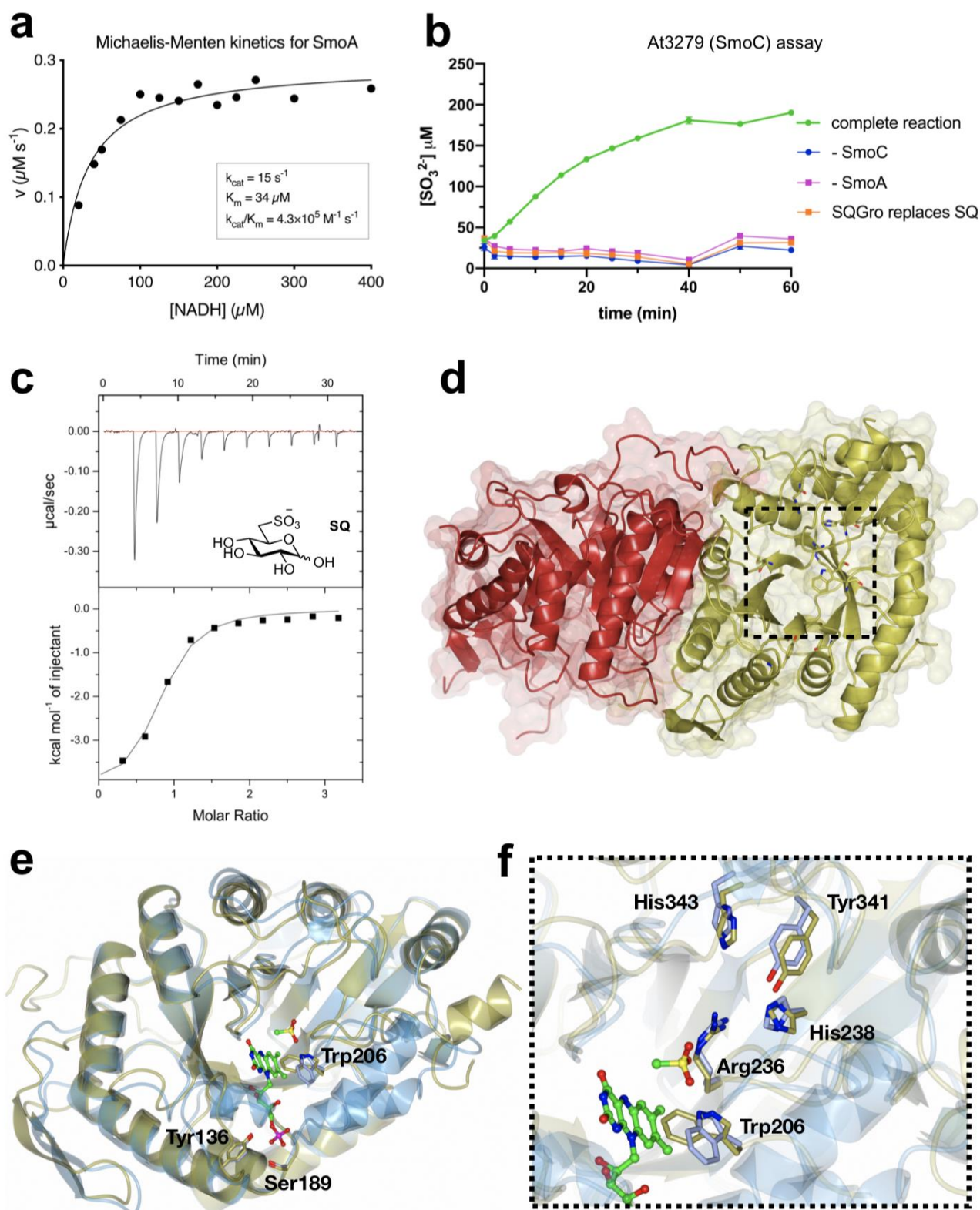


Figure 3: Biochemical and structural analyses of the flavin reductase SmoA and SQ monooxygenase SmoC. (a) Michaelis-Menten kinetics for SmoA-catalysed reduction of FMN by NADH (b) SmoC activity assessed using sulfite release assay with Ellman's reagent in the presence of FMN, flavin reductase, NADH and SQ. (c) Isothermal titration calorimetry of interaction of SmoC with SQ as determined by ITC. (d) Transparent molecular surface and ribbon diagram of *RoSmoC* homodimer showing cofactor binding pocket and active site. (e) Overlay of *RoSmoC* (in

926 gold) and MsuD·FMN·CH₃SO₃⁻ complex (7K14.pdb in ice blue) showing location of FMN pocket.
927 (f) Overlay of *RoSmoC* (in gold) and MsuD (7K14.pdb in ice blue) showing detailed view of proposed
928 substrate-binding pocket and conserved residues lining the active site of *RoSmoC*.

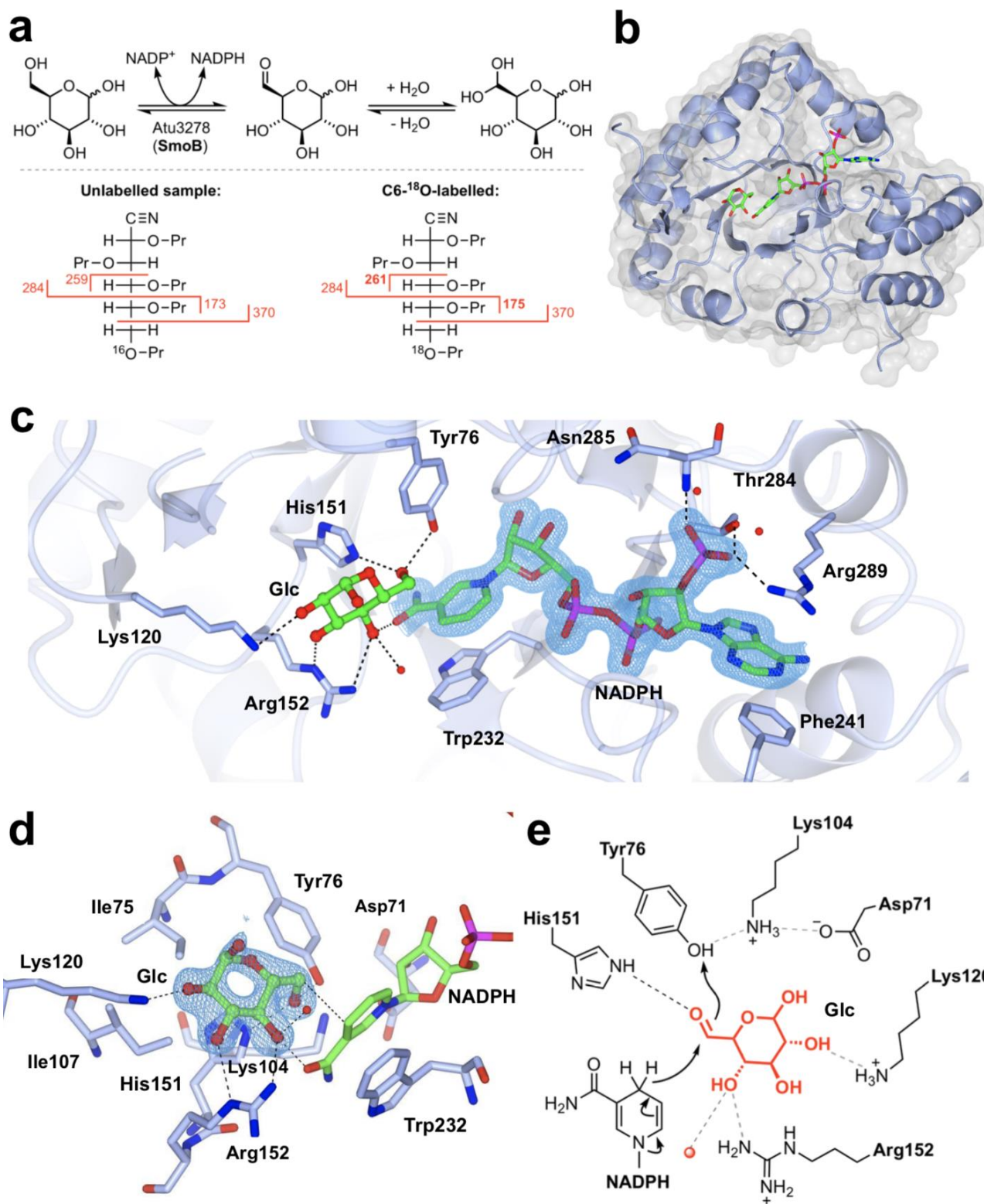


Figure 4: Biochemical and structural analyses of 6-oxo-glucose reductase SmoB. (a) Top: Equilibrium oxygen exchange at C-6 of Glc via 6-OG facilitated by SmoB when incubated with NADP⁺ in H₂¹⁸O. Bottom: Derivatization and MS fragmentation allows localization of ¹⁸O to C6 of Glc. (b) Transparent molecular surface and ribbon diagram of SmoB in complex with NADPH and Glc. (c) Closeup view of SmoB•NADPH•Glc ternary complex. Backbone and carbon atoms of SmoB are shown in ice blue and NADPH and glucose are shown in cylinder format. Electron density for

936 NADPH corresponds to the 2Fo – Fc map in blue at levels of 1 σ . (d) Substrate binding pocket of
937 SmoB depicting hydrogen bonding interactions of glucose with the active site residues including the
938 conserved catalytic residues Asp71, Lys 104, His151 and Tyr76. Electron density corresponds to the
939 2Fo – Fc map (in blue) at levels of 1 σ . The geometry of the SmoB-Glc complex indicates the likely
940 trajectory of hydride addition to 6-OG. (e) Proposed mechanism of SmoB catalyzed reduction of 6-
941 OG by NADPH showing hydride transfer from C4 of nicotinamide ring of NADPH to C6 carbonyl
942 and Y76 (within the catalytic tetrad) as the proton donor. The red sphere is a bound water molecule;
943 dotted lines are proposed hydrogen bonds.

